Author/s:
Ren, J;Guo, S-Y;Zhao, T-J;Chen, J-Z;San Nicolas, R;Zhang, L

Title:
Constructing a novel nano-TiO2/Epoxy resin composite and its application in alkali-activated slag/fly ash pastes

Date:
2020-01-30

Citation:
Ren, J., Guo, S. -Y., Zhao, T. -J., Chen, J. -Z., San Nicolas, R. & Zhang, L. (2020). Constructing a novel nano-TiO2/Epoxy resin composite and its application in alkali-activated slag/fly ash pastes. Construction and Building Materials, 232, https://doi.org/10.1016/j.conbuildmat.2019.117218.

Persistent Link:
https://hdl.handle.net/11343/292049

Total wordcount:8807

Constructing a novel nano-TiO_2/Epoxy resin composite and its application in alkali-activated slag/fly ash pastes

Jie Ren[1,2,3], Si-Yao Guo[1,2*], Tie-Jun Zhao[1,2], Ji-Zhou Chen[1,2], Rackel San Nicolas[3], Lihai Zhang[3]

1 School of Civil Engineering, Qingdao University of Technology, Qingdao, 266033, China

2 Collaborative Innovation Center of Engineering Construction and Safety in Shandong Blue Economic Zone, Qingdao, 266000, China

3 Department of Infrastructure Engineering, the University of Melbourne, Victoria, 3010, Australia

Abstract:

A novel in-situ synthetic method is developed for fabrication of inorganic-organic hybrid structured TiO_2/Epoxy resin composite without adding any surfactants. It is discovered for the first time that the inorganic-organic micro-structured TiO_2/Epoxy composite can be homogeneously dispersed in one type of alkali-activated binders: alkali-activated slag/fly ash (AASF) pastes with slag/fly ash at 50/50. Besides, it is found that TiO_2/Epoxy composite is capable of enhancing the mechanical properties including compressive and flexural bending strengths, improving porous structures and reducing drying shrinkage of the AASF paste. Moreover, scanning electron microscopy results showed that the AASF binder enhanced by TiO_2/Epoxy resin composite has a smooth and flat morphology with fewer cracks as compared to the control paste, leading to a denser microstructure. It is assumed that both TiO_2 and epoxy resin are beneficial in improving the microstructure and hence the macroscopic properties of AASF binders were also improved. Since the preparation of TiO_2/Epoxy composite through in-situ polymerization method is attractive because of its simple manufacturing procedure and cost-effectiveness, its modified AASF binders have an

appealing potential to be used for large-scale production and field applications in the foreseeable future.

Keywords: Nano-TiO_2/epoxy resin composite; In-situ preparation; Alkali-activated slag/fly ash binders; Mechanical properties; Microstructure; Shrinkage

1. Introduction

The global production of cement has grown rapidly in the past few decades, and with the annual cement production of about 2.8 billion tonnes which is projected to reach 4 billion tonnes per year [1], it is the third-largest source of anthropogenic CO_2 emissions. Due to the decomposition of carbonates, cement manufacturing factories emit large amounts of gaseous pollutants such as CO_2, SO_2 and NO_X, which are the main cause of the greenhouse effect and the formation of acid rain [2, 3]. Therefore, to find out an alternative which can replace ordinary Portland cement (OPC)-based materials is a critical concern in addressing the issue of anthropogenic global climate change. Alkali-activated cement (also known as inorganic polymer cement) is a newly developed cementitious material prepared by using industrial wastes (such as granulated blast furnace slag, fly ash, even waste clay brick powder etc.) as raw materials [4-7]. They are attracting more attention and considered as a promising potential binder to replace OPC-based binders because of many properties comparable or even superior to traditional OPC-based materials, such as high early mechanical strength [6, 8], corrosion resistance [9, 10], stabilization of toxic wastes [11]. In addition, the manufacturing process is relatively simple, with low carbon dioxide footprint and small pollution [12, 13]. For example, unlike OPC, the manufacturing of alkali-activated cement is not subjected to calcination of limestone and sintering of raw materials at high temperatures (usually between 1300-1450 ℃) [14], thus saving a lot of energy and improving environmental sustainability. Therefore, alkali-activated cement based concretes have

become increasingly appealing in the field of cementitious materials in recent years. Within the alkali-activated binders, alkali-activated slag/fly ash (AASF) binders are becoming more attractive due to their unique characteristics which cannot be achieved by using a single raw material as the sole precursor [15-21].

Nevertheless, further advances in a wider large-scale application of alkali-activated binders are limited due to relatively higher brittleness than their OPC counterparts because of their binding system which is similar to ceramic-based crosslinked structures [6]. To tackle this problem, various materials have been used to improve the high brittleness and poor toughness of alkali-activated binders, such as high-performance short fibers, nano-particles and organic-based composites [22-26] or even SiC as the foaming agent to obtain a porous composite [27]. However, most of these materials are based on the modification methods of cement and ceramics, whereas no effective chemical bonding between modifiers and alkali-activated binders matrix is formed.

Organic-inorganic materials have recently attracted a lot of attention due to their excellent properties [28-31]. The most advantageous feature of these materials is that they can be conveniently designed and equipped with properties that are difficult to achieve in either organic or inorganic materials alone. For instance, compared with many conventional materials, emerging organic-inorganic materials exhibit properties such as dimensional stability and thermostability stemming from the inorganic phase [32] as well as the characteristics such as an improved viscoelasticity derived from the organic phase [33]. Epoxy resin is an important high-molecular weight material with high thermal stability, density and viscosity as well as a relatively low cost. In recent years, TiO_2 modified epoxy resin is of large interest because it can not only improve the brittleness effectively, but also offer good aging resistance for epoxy resin [34-37]. Hence, more efficient functions of epoxy resin are achieved. Given limited research on the TiO_2/Epoxy resin systems and their

applications to inorganic materials, in this study, we report for the first time a novel inorganic-organic structured nano-TiO_2/Epoxy resin composite for modifying AASF binders. The aim of this study is to investigate the influences of the TiO_2/Epoxy resin on the flowability, mechanical properties, porous structures and shrinkage behaviors of the AASF and related mechanisms. Several possible explanations are proposed based on the experimental results and microstructural analysis.

2. Experimental methods

2.1. Raw materials for AASF binder

A class F fly ash (FA) and ground granulated blast furnace slag (GGBFS) were used in this study as the precursors for the AASF paste manufacturing. FA used was supplied by Cement Australia Ltd., and the GGBFS was produced by Australian Builders Ground Slag. Their oxide compositions obtained by X-ray fluorescence are presented in Table 1. FA has a specific gravity at 2200 kg/m^3 and a median particle size at 25 μm. In addition, the Blaine fineness of FA is 410 ± 10 m^2/kg. The specific gravity and median particle size of GGBFS is 2800 kg/m^3 and 14 μm respectively with particle size ranging between 0.1 and 74 μm, determined by laser granulometric analysis.

Table 1.

Chemical compositions of the GGBFS and FA used in this study (% by mass), as determined by X-ray fluorescence. LOI is loss on ignition at 1,000 ℃.

Oxide	SiO_2	TiO_2	Al_2O_3	Fe_2O_3	MnO	MgO	CaO	K_2O	P_2O_5	SO_3	LOI
GGBFS	31.00	0.49	13.96	0.32	0.33	6.33	40.92	0.31	0.01	2.17	2.11
FA	42.09	1.44	25.13	13.16	0.18	1.27	13.56	0.41	1.10	0.41	0.81

2.2. Synthesis of the TiO_2 and TiO_2/Epoxy resin composites

2.2.1. Synthesis of TiO_2

In this study, 10 mL $Ti(OC_4H_9)_4$ was dissolved in 20 mL anhydrous ethanol to form the solution A. After that 10 mL anhydrous ethanol, 1.8 mL distilled water and 4.2 mL acetic acid with a certain amount of phosphoric acid were mixed together to form the solution B. Solution B was subsequently added dropwise into solution A with vigorous stirring to form a homogeneous mixture which lasted 6 hours until $Ti(OC_4H_9)_4$ was completely hydrolysed. Then the mixture was transferred to Teflon-lined stainless steel autoclave and subjected to hydrothermal treatment at 200 ℃ for 12 hours. Finally, the powder sample was gravity filtered, rinsed with ethanol and deionized water, and dried at 60 ℃ for another 12 hours.

The appearance of the dried TiO_2 nanoparticles in clusters is shown in in Fig. 4. Besides, a scanning electron microscopy (SEM) image showing the morphology of TiO_2 nanoparticles is presented in Fig. 5.

2.2.2. Synthesis of TiO_2/Epoxy resin composite

Firstly, the Bisphenol-A (CAS 85-05-7) and 1-chloro-2,3-epoxypropane, also known as epichlorohydrin was added into a four-necked reaction flask equipped with a mixer and thermometer. The mixture was then subjected to water-bathing at 75 ℃ and agitated until the reactants were fully dissolved followed by cooling down naturally in ambient environments to 70 ℃. After that, 40 mL 20% (by mass) NaOH aqueous solution containing 5% (by mass) TiO_2 used as dispersion medium was added drop by drop within 0.5 h. Then the mixtures continuously reacted for another 1.5-2 hours with a controlled temperature at 75-80 ℃ until the solution changed into creamy yellow colour. The reaction time and temperature selected were based on the previous experiments. Then the heating process was stopped, and the mixture was allowed to cool down naturally. 60 mL Benzene was then added into the mixture and stirred. The resin solution was transferred to a separatory funnel, standing for a while and

the lower water layer was removed. The rest solution was washed by deionized water for many times until the wash water became neutral indicated by a pH meter. Chloride ion was also tested using silver nitrate ($AgNO_3$) solution. Finally, the organic layer was collected. The upper layer of benzene was poured into a vacuum distillation unit and distilled at 75 ℃ with a normal pressure. After this, all volatile matters in the vacuum distillation were removed and the rest TiO_2/epoxy resin composite was poured out and stored properly.

2.3. Preparation of AASF composited with TiO_2-Epoxy resin

The alkaline activator used was prepared by adding a solid anhydrous sodium metasilicate Na_2SiO_3 (Na_2O:SiO_2 molar ratio at 1:1 supplied by Redox Pty Ltd.) into distilled water and then stirred for at least five minutes. Due to the release of heat while mixing the sodium metasilicate and the curing temperature effect on the reaction products of the AASF binder [38], the mixture solution was then allowed to cool down naturally until reaching the room temperature (23 ± 2 ℃) in the ambient environment prior to the following procedures [39].

The ready-prepared TiO_2/Epoxy resin liquid was then poured into the premixed alkaline activator, and the mixed liquid solution was stirred by a vertical stirrer in a glass beaker for 5 minutes followed by sonication (Branson Ultrasonics™ Fisher Scientific) for another 5 minutes. These approaches were taken under the ambient laboratory environment prior to the preparation of AASF paste samples. The stirring and sonication process is necessary to ensure a well-mixed homogenization of the mixed liquid solution, as shown in Fig. 6.

In order to prevent possible agglomeration and self-stratification of the mixed solution (TiO_2/Epoxy resin and alkaline activator), the homogeneous liquid mixture (Fig. 6) was soon added into the slag/fly ash solid precursor which was already mixed first for two minutes. Then the combined mixture was mixed using a planetary Hobart mixer (5 l in capacity) for 8 minutes before casting. The fresh pastes were cast in two layers into 50 mm cubic moulds for compressive strength test. The pastes for flexural bending strength were cast into 40 mm × 40

mm ×160 mm steel moulds. During the casting process, each layer was compacted on a vibrating table for about 2-3 minutes to remove entrapped air bubbles. After casting, all samples were fully covered with a plastic film and demoulded after 24 hours. Then, all samples were tightly sealed in plastic bags to minimise moisture loss and cured in room temperature (23 ± 2 ℃) until the day of testing. The same ratio and amount of binder (GGBFS + FA) but without addition of the TiO_2/Epoxy resin composite was applied for the control mix, namely pure AASF paste which is denoted as 'Control'. The mix proportions of the two paste mixes are shown in Table 2. A schematic diagram showing the preparation and manufacturing process of the TiO_2/Epoxy resin composited AASF paste is shown in Fig. 1.

Table 2.

Mix proportions of the paste samples used in the study.

Sample ID	GGBFS/FA mass ratio (%)	Activator [a] (solid powder)	Water[a]	TiO_2/Epoxy resin[a]
TiO_2/Epoxy	50:50	8.0	34.2	2
Control	50:50	8.0	34.2	NA

[a] all ratios are expressed as the mass percentage (%) ratio compared to the binder content. The total binder content (GGBFS+FA) is 1500 kg/m^3. NA-Not available.

2.4. Characterisation of TiO_2-Epoxy resin composited AASF pastes

2.4.1. Measurements of flowability and mechanical properties

The flowability of the newly-mixed pastes was tested by performing mini slump test, which was also used by other researchers [40, 41]. In accordance with ASTM: C1437 [42], the newly mixed pastes with and without the TiO_2/Epoxy resin, before casting into the moulds, were poured into the truncated conical mould (top diameter = 70 mm, bottom diameter = 100 mm, height = 50 mm). A layer with about 25 mm thickness was formed and then tamped 20 times using a tamper. Later on, another layer of fresh paste was immediately poured into the

conical mould as specified for the first layer. After that, the top surface of the mould was levelled by removing all extra pastes. Then the conical mould was lifted vertically, and the diameters of the paste spread was measured along the two perpendicular directions which are marked on the round vibrating table. The relative slump value was obtained from Eq.(1) [43]:

$$\Gamma p = \left(\frac{d}{d_0}\right)^2 - 1 \quad (1)$$

where Γp is relative slump, d is the average value of the two measured diameters of the paste spread, and d_0 is the diameter of the bottom of the conical cone, which is 100 mm in this test [15].

Compressive strength test was conducted on cubic samples (50 mm × 50 mm × 50 mm) according to ASTM C109M [44]. Pastes specimens were loaded at a fixed rate (0.9 kN/s) until sample failure using a compression testing machine (ELE International). Paste samples for compressive strength test were cured for different curing ages (7-day, 28-day, 56-day and 90-day) to monitor the evolution of compressive strength. For each mixture at each testing time, the mean value of three samples was expressed as the final result. This test provides a macroscopic indication of the effect of TiO_2/Epoxy resin composite on the mechanical properties of the AASF pastes.

Flexural bending strength was also determined by following the standard AS 1012.11-2000 [45]. The testing machine as shown in Fig. 2 has a displacement loading rate at 1.2 mm/min employed to conduct the measurements. Similar method was also used in another study [46]. Three rectangular sample bars of each mixture with a dimension of 40 mm × 40 mm × 160 mm were subjected to the three-point bending test and the averaged value was reported as the final results. The flexural strength (σ_F) was then calculated using Eq.(2):

$$\sigma_F = \frac{3}{2}\frac{P_m S}{B W^2} \quad (2)$$

where P_m is the maximum load at crack extension, S is the span of the sample (the distance between the two supporting ends), which is 100 mm in this study. B is the specimen width (40 mm) and W is the specimen thickness (40 mm) or known as depth. The flexural strengths of paste samples after 7-day, 28-day, 56-day and 90-day were tested. However, only the 56-day and 90-day flexural strengths are presented in the paper since the other corresponding flexural strengths were too low.

2.4.2. Measurements of pore-related properties

The water absorption (%) and the volume of permeable voids (VPV) after 56-day curing were measured on cylindrical samples (27.5 mm in diameter and 55 mm in height) through a modified version of ASTM C642-06 [47]. In this case, paste samples were preconditioned in an oven with a temperature at 60 ℃ until the weight became constant [48]. This procedure was modified and different from the one specified in ASTM C642-06 which requires the temperature of drying samples at 100-110 ℃ until a constant mass is obtained. This temperature range has been reported to cause significant changes in porous structures of the alkali-activated binders and can even induce microcracks and severe desiccation of specimens [48, 49]. Then samples were allowed to cool down in a dessicator (23 ± 2 ℃) overnight for at least 24 hours until a constant weight was obtained (denoted as m_i). After that the samples were fully immersed in clean tap water for at least 3 days. While weighing the mass, samples were taken from the clean water, wiped slightly and quickly with a wet cloth to remove the surface water followed by being weighed immediately. The saturated surface-dry mass obtained from this procedure is noted as m_s. After the immersion in water at room temperature, samples were submerged in boiling water for at least 5 hours and the

boiling water was allowed to cool by natural loss of heat until the final water had a room temperature (23 ± 2 ℃). The mass of the samples in boiling water with the same weighing procedure as before is expressed as m_b. Finally, the samples were suspended using a wire and the corresponding apparent mass (m_w) in water was then recorded.

The bulk density of the dry sample (g_1) and the apparent density (g_2) can be calculated based on the following equations Eq. (3) and Eq. (4), respectively.

$$g_1 = m_i / (m_b - m_w) \times \rho \quad (3)$$

$$g_2 = m_i / (m_i - m_w) \times \rho \quad (4)$$

Then the water absorption and volume of permeable voids (VPV) are expressed as:

$$\text{Water absorption (\%)} = (m_s - m_i) / m_i \times 100 \quad (5)$$

$$\text{VPV (\%)} = (g_2 - g_1) / g_2 \times 100 \quad (6)$$

where ρ is the density of pure water which is 1 g/cm^3 in this study. The final results were expressed as the average of three samples.

In this study, the capillary sorptivity test was performed, according to ASTM C1585-04 [50] which is closely associated with the tendency of samples to absorb and transmit water or other liquid via capillary actions. Moreover, it is one of the most important properties to characterise the porous networks such as tortuosity and connectivity, which can reflect the transport mechanism of water or other liquid movement [51]. The disk-shaped cylindrical samples with dimensions of 50 mm in diameter and 8-10 mm in height were first dried in a laboratory oven at 50 ℃ for at least three days until the final mass remained constant. After that, the samples were allowed to cool down in ambient environment (room temperature at 23 ± 2 ℃, RH = 50 ± 20%) for at least 24 hours. Then all peripheral curved surfaces of the samples were sealed by a non-absorbent silica gel as a coating to prevent the ingress of water

from these surfaces and only the bottom surface was able to absorb water. After another 24 hours, all samples were put into a plastic container on a saturated sponge which was fully saturated with tap water. Therefore, all samples were drowned with the water level about 2-3 mm above their bottom. During this process, tap water was replenished into the container to ensure that the sponge was fully saturated and the water level remained the same throughout the test. The quantity of water absorbed from the bottom by samples was recorded at predetermined intervals for up to 8 days. At each measurement, surface water on the specimens was wiped off using a dampened cloth with the weighing operation completed within 30 seconds so as to minimize the loss of water inside the sample due to evaporation. Then the ingress of water per unit area I can be expressed as the following equation:

$$I = \frac{\Delta m_t}{S \times d} \tag{7}$$

where the mass gain of the sample is denoted as Δm_t (g) at each time interval t (min) and S is the bottom area (mm^2) which is the only surface that the water can penetrate. In this case, the bottom area S is 1962.5 mm^2. d is the density of water in g/mm^3. Then the capillary sorptivity Cs can be calculated using the next equation Eq. (8).

$$Cs = \frac{I}{t^{1/2}} \tag{8}$$

Specifically, there is a linear part between I and $t^{1/2}$ during the initial ingress of water via capillary forces and the slope of this part is considered as the capillary sorptivity ($mm/min^{1/2}$). The test was performed in triplicates for the two paste mixes.

2.4.3. Scanning electron microscopy (SEM)

The morphology of the two mixes after 56-day curing was observed with scanning electron microscopy in secondary electron mode. The equipment used was a Shimadzu SS-550 microscope at 15 keV. Paste samples of the two mixes after 56-day curing were crushed and

then sectioned in epoxy resin followed by being polished carefully. 800-4000 mesh grade SiC abrasive paper was used to polish the sample surface after the resin got hardened and excess resin was removed. For each grade SiC polishing procedure, two minutes were used. After that, they were cleaned with distilled water and dried with compressed air prior to the SEM analysis.

2.4.4. Measurements of drying shrinkage

Early stage shrinkage of the paste after casting is considered as a critical parameter for durability assessment since it is also closely related to capillary pores. Drying shrinkage increases due to the loss of water by hydrostatic tension from some small capillary pores over time [52], leading to the formation of many cracks where different liquid solutions along with aggressive ion species can intrude into. The ingress of these aggressive agents would finally result in partial or complete loss of binder matrix until the total failure of the structures [52]. In this study, drying shrinkage values were obtained by monitoring the length of the paste samples at different during ages.

The initial length of the paste prisms (40 × 40 × 160 mm) was measured after 24 hours of curing at room temperature and then the measurements of length changes after different curing ages were conducted. According to ASTM C157/C157M-08 [53], the samples were sealed with plastic film and placed in a drying room with a temperature at 23 ± 2 ℃ and a relative humidity (RH) at 50 ± 5% throughout the whole testing procedure. The initial length L_i (mm) and the length L_x (mm) after 3, 7, 21 28, 42, 56 and 90 days of curing was measured with a digital comparator. The obtained length after each curing age was an average of three samples. This method was also used by Wenyan Zhang et al. [54] and L.Y. Yang et al. [55] but with slightly different storage regime. The length changes (LC) were then calculated using the following formula:

$$\text{LC(microstrain)} = (L_i - L_x) / G \times 10^6 \quad (9)$$

where G is the nominal effective length which is 160 mm in this study. L_i and L_x is the initial length and the length after specific curing days, respectively. A presentation of shrinkage measurement is shown in Fig. 3.

3. Results and discussion

3.1. Properties of the AASF pastes

3.1.1. Flowability and mechanical strengths

The mini slump test results of the newly-mixed TiO_2/Epoxy and the control pastes are shown in Fig. 7(a) and (b), respectively. As shown in Fig. 7(a), the TiO_2/Epoxy paste sample exhibits a slightly smaller flowability compared to the control sample (Fig. 7(b)), with the averaged spread-flow at 135 mm and 145 mm respectively. The corresponding relative slump Γp obtained from Eq.(1) is approximately 0.82 and 1.10 respectively. These differences can be contributed to the presence of organic TiO_2/Epoxy resin with a high viscosity, making the AASF binder more viscous compared to the control [56]. This increased viscosity of the AASF specimens indirectly implies a homogeneous dispersion of the TiO_2/Epoxy resin composite in the AASF paste.

The 56-day and 90-day mechanical properties of the two binder mixtures are shown in Table 3 and the compressive strength evolution during the 90-day curing period is presented in Fig. 8. It is obvious in Table 3 that the TiO_2/Epoxy sample obtained a higher 56 and 90-day compressive strength compared to the control paste, 65.98 and 68.81 MPa respectively, whereas the compressive strength for the control samples after 56 days and 90 days of curing was 64.33 and 67.01 MPa respectively. Therefore, the 56-day and 90-day compressive strength was increased by 2.56% and 2.69% respectively for TiO_2/Epoxy sample compared to

the control. It is worth pointing out that the data for 56-day compressive strength was also included in another paper [57].

The flexural strength of the two mixes was much lower than the compressive strength. A flexural strength at 2.23 (56-day) and 2.25 MPa (90-day) was recorded for the TiO_2/Epoxy samples and the corresponding values for the control paste was 2.07 (56-day) and 2.08 MPa (90-day). Therefore, an increment in the flexural strength was reported for TiO_2/Epoxy samples which was 7.73% and 8.17% after 56-day and 90-day curing respectively compared to the control pastes. Furthermore, based on the obtained flexural and compressive strength, the flexural-compressive strength ratio was calculated in order to reflect the brittleness of the two paste mixes [58]. It was already confirmed that as the brittleness of a material increases, the flexural-compressive strength decreases [59, 60]. In this study, the flexural-compressive strength ratios of the two paste mixes are also shown in Table 3. It is clear that the flexural-compressive strength ratios of the TiO_2/Epoxy samples irrespective of different curing ages were also larger than those of the control pastes. The load-deflection curve for the two samples after 56-day curing is also depicted in Fig. 9. It can be seen that both two curves show an abrupt decrease in the load after reaching the maximum value indicating an intrinsic ceramic-like fracture behaviour of alkali-activated binders. However, the abrupt descending part in the curve of TiO_2/Epoxy pastes seems to be milder compared to that of pure AASF counterpart. This can be due to the addition of TiO_2/Epoxy resin which to some degree absorbs some energy and the failure mode was thus improved. Based on the area under the load-deflection curve, the absorbed energy (flexural toughness) is calculated which is 0.134 N·m and 0.091 N·m for the TiO_2/Epoxy AASF pastes and normal AASF pastes, respectively. This result corresponds well with the obtained flexural-compressive strength ratios. These results suggest that an improved toughness was achieved for the AASF paste enhanced by the TiO_2/Epoxy resin. It is worth noting that the improvements in the compressive strength and

flexural bending strength were not significant, especially considering the standard deviations. This is likely due to the small amount of addition of TiO_2/Epoxy resin composite which was only 2% (by mass).

Table 3.

The 56-day and 90-day compressive and flexural strengths as well as the corresponding flexural-compressive strength ratios of the two mixes. The standard deviations are expressed in brackets.

Sample ID	TiO_2/Epoxy		Control	
Different curing ages	56-day	90-day	56-day	90-day
Compressive strength (MPa)	65.98 (4.21)	68.81 (2.91)	64.33 (5.78)	67.01 (5.84)
Flexural strength (MPa)	2.23 (0.18)	2.25 (0.15)	2.07 (0.13)	2.08 (0.05)
Flexural-compressive strength ratio (%)	3.38	3.27	3.22	3.10

In addition, as shown in Fig. 8, the compressive strength of the TiO_2/Epoxy paste was larger than that of the control at all curing ages indicating an enhanced mechanical property. Despite the small increments in the compressive strength which can be ascribed to the small amount of TiO_2/Epoxy resin addition as mentioned earlier, the consistent improvement in the compressive strength during the whole curing period suggests that the TiO_2/Epoxy resin is beneficial in improving the mechanical strengths of the AASF paste tested in the study.

The increased compressive strength and flexural strength of the TiO_2/Epoxy sample are in consistent with the experimental findings in many other studies [6, 29, 32] which showed that the epoxy resin-based composite could enhance the mechanical properties of inorganic cementitious binders. The only difference is that in this study the organic epoxy resin was itself enhanced by nano-TiO_2 which also led to an increase in the mechanical strength of the AASF binder. The improved mechanical strengths are closely related to the porous structures of the two mixes which are discussed in the following section.

3.1.2. Pore-related properties

Table 4 shows the results of pore-related properties including water absorption, VPV as well as the capillary sorptivity of the two paste mixes after 56 days of curing. Water absorption reflects the porosity of bulk samples and VPV is based on the test method AS 1012.21 [61]. VPV is one of the most important parameters that can be used to simply evaluate the potential durability of cementitious specimens [62]. It has been reported that VPV has a satisfactory correlation coefficient with chloride diffusion resistance among all various durability test methods [63].

According to Table 4, it is obvious that the TiO_2/Epoxy paste sample had a lower water absorption and VPV, which was 16.14% and 27.31% respectively, compared to the control pastes respectively at 17.77% and 29.64%. This further implies that the addition of TiO_2/Epoxy resin composite into the binder decreased the total volume of pores in the binder matrix, leading to a denser microstructure than that of the control paste. These results correspond well with the increased compressive and flexural strength of the TiO_2/Epoxy sample as compared to the control. The VPV results also indicate that the AASF binder with TiO_2/Epoxy resin addition has a better durability compared to the control AASF pastes.

Table 4.

The pore-related properties of the two paste samples after 56-day curing.

Sample ID	Water absorption (%)	VPV (%)	Capillary sorptivity (mm/min$^{1/2}$)
TiO_2/Epoxy	16.14 (0.02)	27.31 (0.03)	0.074 (0.014)
Control	17.77 (0.01)	29.64 (0.03)	0.350 (0.027)

Fig. 10 demonstrates the cumulative water ingress (mm) against square root of time (min$^{1/2}$). The slope of the initial linear part in Fig. 10 is considered as the capillary sorptivity (mm/min$^{1/2}$), with the results shown in Table 4. Capillary sorptivity provides useful

information about the connectivity and tortuosity of porous microstructures. From Fig. 10, for TiO_2/Epoxy sample, the linear part in the curve was from the beginning to almost 400 minutes (20 $min^{1/2}$) and then it continuously increased with a lower rate within the 24-hour absorption, finalising less than 2.4 mm (ingress of water). In contrast, the control sample underwent its significant linear increase in water ingress within 120 minutes (approximately 11 $min^{1/2}$) and then almost had no substantial increment, reaching more than 4.8 mm (ingress of water) at the end of 24-hour capillary sorptivity test. According to the final results in Table 4, it can be seen that the capillary sorptivity of the TiO_2/Epoxy sample (0.074 mm/$min^{1/2}$), was significantly reduced compared to that of the control (0.350 mm/$min^{1/2}$). These results suggest that there was a much less interconnected capillary network in the TiO_2/Epoxy pastes than the control and that the total volume of capillary pores was also decreased [52] as evidenced by the final ingress of water at the end of 24 hours of measurement. Thus, it is obvious that the addition of TiO_2/Epoxy resin significantly improved the porous structure as compared to the control AASF without the TiO_2/Epoxy resin enhancement. These results were also reported in other studies which confirmed the pore-occupying nature of epoxy resin based additives [64-66]. It is worth pointing out that the hydrophobic character of epoxy resin may also reduce the capillary sorptivity, which merits further investigation.

Based on these experimental results and previous studies [57, 63, 67], it can be assumed that the TiO_2/Epoxy AASF binder would have a higher resistance against acid or other aggressive solutions due to their less interconnected and more tortuous porous structure as well as a lower volume of pores. For instance, it was already confirmed that the AASF binder (slag/FA ratio at 50:50) composited with TiO_2/Epoxy resin displayed a higher phosphoric acid resistance, especially when subjected to drying-wetting cycles [57]. The durability performance of the two binder mixes requires further investigations which is not the focus in this study.

3.1.3. Morphology analysis

Fig. 11 shows the SEM micrographs of the newly formed TiO_2/Epoxy AASF and control samples. It is apparent that the TiO_2/Epoxy AASF paste has a relatively smooth and flat morphology with only a few microcracks, as shown in Fig. 11(a). In comparison, control sample shows more microcracks on the surface, indicating obvious defects in the matrix structure (Fig. 11(b)). It was already reported that for AASF containing 50% slag and 50% FA, it has a similar structure as alkali-activated slag binder with the C-A-S-H as the main binding gel [18, 68]. Therefore, this phenomenon corresponds well with the findings in other research that alkali-activated slag binders are often subjected to drying shrinkage [55, 69-71]. The SEM images therefore suggests that the TiO_2/Epoxy composites can efficiently limit the formation and development of cracks, leading to a denser microstructure as compared to the control matrix. The SEM results are also in good agreement with the pore-related properties including water absorption, VPV and capillary sorptivity. Further, the bulk samples of the two mixes are also shown in Fig. 11 below the SEM images. It seems that the TiO_2/Epoxy AASF sample displays a smoother surface compared to the control paste.

3.1.4. Drying shrinkage

The drying shrinkage values of both two mixes during the 90-day curing time are presented in Fig. 12. It is apparent that the shrinkage of the TiO_2/Epoxy sample and the control sample both increased significantly during the 60 days of curing and then levelled off, reaching at about 3560 and 4050 micro strain respectively after 90 days of curing. It can also be seen from the figure that the shrinkage value of the TiO_2/Epoxy sample was much smaller than that of the control pastes, especially within 21 days of curing.

The percent reduction in the shrinkage of the TiO_2/Epoxy sample compared to the control is calculated and shown in Table 5. It is apparent that a shrinkage reduction upto about 76.0%

and 56.6% was observed after 3 and 7 days of curing respectively. Considering the less interconnected capillary networks in the AASF binder matrix evidenced by the low capillary sorptivity in *Section 3.1.2*, the reduced drying shrinkage of the TiO_2/Epoxy sample can be attributed to a delayed loss of water [52]. In addition, it is worth noting that the reduction in the drying shrinkage gradually decreased as the curing regime proceeded (Table 5). For instance, the percent reduction in the shrinkage dropped to approximately 16.1% and 12.1% after 56 and 90 days of curing respectively. This can be explained by considering the fact that the water-induced hydrostatic tension effect [52], which is the main reason for shrinkage, is no longer significant during the later stage of curing as there was less evaporable water in the binder after a long-term curing. This also explains why the total shrinkage gradually had no significant increase, reaching a plateau after about 60 days of curing. The measured smaller shrinkage value of the TiO_2/Epoxy sample would lead to fewer cracks which is also consistent with the SEM images as shown in Fig. 11. Fewer cracks suggest that a denser TiO_2/Epoxy binder was obtained and a higher resistance towards the ingress of aggressive ion species (e.g. sulphate and chloride) can be expected as a comparison to the normal AASF binder. Further research is necessary to explore the durability of the two mixes when exposed to various aggressive conditions.

Table 5.

The percent reduction (%) in the drying shrinkage of TiO_2/Epoxy paste in comparison with the control paste during 90-day curing ages.

Curing ages (Days)	3	7	21	28	42	56	90
Percent reduction (%)	76.02	56.59	36.82	28.01	21.27	16.08	12.10

3.2. Related mechanisms

Based on the above experimental results, it can be concluded that the addition of TiO_2/Epoxy resin composite can improve the microstructure of the AASF binder matrix

evidenced by its lower water absorption, VPV and capillary sorptivity. The improved microstructure of the AASF due to the TiO_2/Epoxy resin addition then led to a smaller shrinkage, which results in fewer microcracks as evidenced from the SEM images. Thus, enhanced mechanical properties including compressive and flexural tensile strength compared to the normal AASF paste were obtained.

For compressive strength, it is closely related to the microcracks and air voids distributed and propagated in the samples [51]. The shrinkage results indicate that the incorporation of the TiO_2/Epoxy resin was able to immobilize water molecules to some degree, leading to a delayed evaporation of free water [22]. As a result, there were much fewer microcracks and air voids in the TiO_2/Epoxy samples compared to the control AASF binder which led to an increase in the compressive strength. As for the flexural bending strength, the increase can be explained by considering the two possible roles played by the inorganic-organic TiO_2/Epoxy resin composite. One is that the composite could absorb a certain amount of energy induced by the load via plastic deformation, and another is a toughening effect known as a typical crack deviation mechanism [72]. Crack deflection mechanism typical for ceramic matrix composite enhanced by particles, e.g. TiO_2, may also exist which leads to a slow crack growth and propagation [73, 74]. Moreover, it has been reported that the formation process of some natural organic-inorganic composites resembles the geopolymer production [24]. It has been previously confirmed that biopolymer accelerated sol-gel process and was able to influence the microscopic morphology of the obtained hybrid material. This finally led to a modification of the geopolymerization process and the corresponding promotion of the mineralization [75, 76]. Thus, it is reasonable to assume that epoxy resin polymer enhanced with nano-TiO_2 particles could also contribute to the formation of cross-linking networks with a certain number of organic moieties through sol-gel process. Further research is required to confirm this assumption. In addition, it was reported that there is a large number

of hydrogen bonds between silanol groups and absorbed water bonded to the inorganic backbones in the alkali-activated binder matrix [77]. Some other studies also confirmed the presence of silanol groups and bound water in the fly ash-based alkali-activated binders based on the FTIR results [78-80]. Therefore, the formation of hydrogen bonds may also take place between silanol groups and/or bound water in AASF matrix and hydroxyls in the epoxy resin molecules. Accompanied with the condensation of silanol groups which produces a -Si-O-Al-O-Si- three dimensional cross-linking network at the end of geopolymerization process, a denser microstructure is hence obtained, finally leading to the improved mechanical properties of AASF binders.

4. Conclusions

For the first time, an organic-inorganic structured nano-TiO_2/Epoxy resin composite was well prepared by a facile in-situ synthetic method without using any surfactants, which was then used in the modification of AASF pastes with an addition of 2% (by mass). Several conclusions can be drawn based on the experimental study:

(1) The addition of nano-TiO_2/Epoxy resin composite enhanced the compressive and flexural strength of the AASF paste as well as flexural toughness evidenced by an increased flexural-compressive strength ratio;

(2) For the TiO_2/Epoxy sample, water absorption and VPV was lower than that of the control pastes. Besides, capillary sorptivity was significantly decreased due to the addition of TiO_2/Epoxy resin indicating a more densified and less interconnected microstructure;

(3) The drying shrinkage of the TiO_2/Epoxy samples was smaller than the control pastes cured under 23 ± 2 ℃ and 50 ± 5% RH, and it was remarkably reduced within the 21 days of curing. The reduced shrinkage led to fewer microcracks as shown in the morphology analysis from SEM images;

(4) The inorganic-organic TiO_2/Epoxy resin with a simple in-situ manufacturing process is able to improve the properties of AASF even with a small addition, making AASF binders a more promising alternative to OPC-based counterparts.

5. Acknowledgements

This work was supported by the National Natural Science Foundation of China (51978354), China Postdoctoral Science Foundation Funded Project (2016M600527). The first author would like to express his great thanks to Chinese Scholarship Council (CSC) for financial support and the University of Melbourne as well as Australian Research Council (IH150100006) for providing basic laboratory conditions. The China Ministry of Science and Technology under Grant 2015CB655100, and Major International Joint Research Project under Grant 51420105015 are gratefully acknowledged. The corresponding author also would like to acknowledge the fellowship support received from the Tai Shan Scholar Programme, Open Fund of Key Laboratory of Urban Underground Engineering of Ministry of Education (TUE2017-03).

6. References

1. WBCSD, I., *Cement Technology Roadmap 2009: carbon emissions reductions up to 2050.* World Business Council for Sustainable Development and International Energy Agency.< http://wbcsdcement. org/pdf/technology/WBCSD-IEA_Cement% 20Roadmap. pdf, 2009.
2. Hendricks, C., E. Worrell, L. Price, N. Martin, and L. Ozawa Meida, *Greenhouse Gases from Cement Production, prepared for the IEA Greenhouse Gas R&D Programme.* Utrecht, The Netherlands, ECOFYS, 1999.
3. Anand, S., P. Vrat, and R. Dahiya, *Application of a system dynamics approach for assessment and mitigation of CO2 emissions from the cement industry.* Journal of environmental management, 2006. **79**(4): p. 383-398.
4. Tuyan, M., Ö. Andiç-Çakir, and K. Ramyar, *Effect of alkali activator concentration and curing condition on strength and microstructure of waste clay brick powder-based geopolymer.* Composites Part B: Engineering, 2018. **135**: p. 242-252.
5. Xu, H. and J.S. Van Deventer, *Effect of source materials on geopolymerization.* Industrial & Engineering Chemistry Research, 2003. **42**(8): p. 1698-1706.
6. Ferone, C., G. Roviello, F. Colangelo, R. Cioffi, and O. Tarallo, *Novel hybrid organic-geopolymer materials.* Applied Clay Science, 2013. **73**: p. 42-50.

7. Oh, J.E., P.J.M. Monteiro, S.S. Jun, S. Choi, and S.M. Clark, *The evolution of strength and crystalline phases for alkali-activated ground blast furnace slag and fly ash-based geopolymers.* Cement and Concrete Research, 2010. **40**(2): p. 189-196.
8. Davidovits, J., *Geopolymer, Green Chemistry and Sustainable Development Solutions: Proceedings of the World Congress Geopolymer 2005*. 2005: Geopolymer Institute.
9. Allahverdi, A. and F. Skvara, *Nitric acid attack on hardened paste of geopolymeric cements, Part 1*. CERAMICS SILIKATY, 2001. **45**: p. 81-88.
10. Allahverdi, A. and F. Skvara, *Sulfuric acid attack on hardened paste of geopolymer cements-part 2. Corrosion mechanism at mild and relatively low concentrations.* CERAMICS SILIKATY, 2006. **50**(1): p. 1.
11. Yunsheng, Z., S. Wei, C. Qianli, and C. Lin, *Synthesis and heavy metal immobilization behaviors of slag based geopolymer.* Journal of hazardous materials, 2007. **143**(1-2): p. 206-213.
12. Van Jaarsveld, J., J. Van Deventer, and L. Lorenzen, *The potential use of geopolymeric materials to immobilise toxic metals: Part I. Theory and applications.* Minerals Engineering, 1997. **10**(7): p. 659-669.
13. Provis, J.L. and J.S.J. Van Deventer, *Geopolymers: structures, processing, properties and industrial applications*. 2009: Elsevier.
14. Shi, H., Y. Zhao, and W. Li, *Effects of temperature on the hydration characteristics of free lime.* Cement and concrete research, 2002. **32**(5): p. 789-793.
15. Shang, J., J.-G. Dai, T.-J. Zhao, S.-Y. Guo, P. Zhang, and B. Mu, *Alternation of traditional cement mortars using fly ash-based geopolymer mortars modified by slag.* Journal of Cleaner Production, 2018. **203**: p. 746-756.
16. Nath, P. and P.K. Sarker, *Effect of GGBFS on setting, workability and early strength properties of fly ash geopolymer concrete cured in ambient condition.* Construction and Building Materials, 2014. **66**(Supplement C): p. 163-171.
17. Ismail, I., S.A. Bernal, J.L. Provis, R. San Nicolas, D.G. Brice, A.R. Kilcullen, S. Hamdan, and J.S. van Deventer, *Influence of fly ash on the water and chloride permeability of alkali-activated slag mortars and concretes.* Construction and Building Materials, 2013. **48**: p. 1187-1201.
18. Ismail, I., S.A. Bernal, J.L. Provis, R. San Nicolas, S. Hamdan, and J.S.J. van Deventer, *Modification of phase evolution in alkali-activated blast furnace slag by the incorporation of fly ash.* Cement and Concrete Composites, 2014. **45**: p. 125-135.
19. Lee, N. and H. Lee, *Reactivity and reaction products of alkali-activated, fly ash/slag paste.* Construction and Building Materials, 2015. **81**: p. 303-312.
20. Lee, N., J. Jang, and H. Lee, *Shrinkage characteristics of alkali-activated fly ash/slag paste and mortar at early ages.* Cement and concrete composites, 2014. **53**: p. 239-248.
21. Xie, J., J. Wang, R. Rao, C. Wang, and C. Fang, *Effects of combined usage of GGBS and fly ash on workability and mechanical properties of alkali activated geopolymer concrete with recycled aggregate.* Composites Part B: Engineering, 2019. **164**: p. 179-190.
22. Zhang, Y.J., S. Li, B.Q. Wang, G.M. Xu, D.F. Yang, N. Wang, H.C. Liu, and Y.C. Wang, *A novel method for preparation of organic resins reinforced geopolymer composites.* Journal of materials science, 2010. **45**(5): p. 1189-1192.
23. Zhang, Z.-h., X. Yao, H.-j. Zhu, S.-d. Hua, and Y. Chen, *Preparation and mechanical properties of polypropylene fiber reinforced calcined kaolin-fly ash based geopolymer.* Journal of Central South University of Technology, 2009. **16**(1): p. 49-52.

24. Zhang, S., K. Gong, and J. Lu, *Novel modification method for inorganic geopolymer by using water soluble organic polymers.* Materials letters, 2004. **58**(7-8): p. 1292-1296.
25. Dias, D.P. and C. Thaumaturgo, *Fracture toughness of geopolymeric concretes reinforced with basalt fibers.* Cement and concrete composites, 2005. **27**(1): p. 49-54.
26. Assaedi, H., F. Shaikh, and I.M. Low, *Characterizations of flax fabric reinforced nanoclay-geopolymer composites.* Composites Part B: Engineering, 2016. **95**: p. 412-422.
27. Bai, C., J. Zheng, G.A. Rizzi, and P. Colombo, *Low-temperature fabrication of SiC/geopolymer cellular composites.* Composites Part B: Engineering, 2018. **137**: p. 23-30.
28. Zuo, Y., J. Xiao, J. Wang, W. Liu, X. Li, and Y. Wu, *Preparation and characterization of fire retardant straw/magnesium cement composites with an organic-inorganic network structure.* Construction and Building Materials, 2018. **171**: p. 404-413.
29. Colangelo, F., G. Roviello, L. Ricciotti, C. Ferone, and R. Cioffi, *Preparation and characterization of new geopolymer-epoxy resin hybrid mortars.* Materials, 2013. **6**(7): p. 2989-3006.
30. Wang, X., S. Zhai, and T. Xie, *Mechanism behind the improvement of coupling agent in interface bonding performance between organic transparent resin and inorganic cement matrix.* Construction and Building Materials, 2017. **143**: p. 138-146.
31. Saparov, B. and D.B. Mitzi, *Organic–inorganic perovskites: structural versatility for functional materials design.* Chemical reviews, 2016. **116**(7): p. 4558-4596.
32. Hussain, M., R. Varely, Y. Cheng, Z. Mathys, and G. Simon, *Synthesis and thermal behavior of inorganic–organic hybrid geopolymer composites.* Journal of applied polymer science, 2005. **96**(1): p. 112-121.
33. Lee, A. and J.D. Lichtenhan, *Thermal and viscoelastic property of epoxy–clay and hybrid inorganic–organic epoxy nanocomposites.* Journal of Applied Polymer Science, 1999. **73**(10): p. 1993-2001.
34. Kumar, K., P.K. Ghosh, and A. Kumar, *Improving mechanical and thermal properties of TiO2-epoxy nanocomposite.* Composites Part B: Engineering, 2016. **97**: p. 353-360.
35. Huang, K., Y. Nien, J. Chen, T. Shieh, and J. Chen, *Synthesis and properties of epoxy/TiO2 composite materials.* Polymer composites, 2006. **27**(2): p. 195-200.
36. Radoman, T.S., J.V. Džunuzović, K.B. Jeremić, B.N. Grgur, D.S. Miličević, I.G. Popović, and E.S. Džunuzović, *Improvement of epoxy resin properties by incorporation of TiO2 nanoparticles surface modified with gallic acid esters.* Materials & Design (1980-2015), 2014. **62**: p. 158-167.
37. Bezy, N.A. and A.L. Fathima, *Effect of TiO2 nanoparticles on mechanical properties of epoxy-resin system.* Int J Eng Res Gen Sci, 2015. **3**(5): p. 143-151.
38. Kubba, Z., G. Fahim Huseien, A.R.M. Sam, K.W. Shah, M.A. Asaad, M. Ismail, M.M. Tahir, and J. Mirza, *Impact of curing temperatures and alkaline activators on compressive strength and porosity of ternary blended geopolymer mortars.* Case Studies in Construction Materials, 2018. **9**: p. e00205.
39. Aiken, T.A., W. Sha, J. Kwasny, and M.N. Soutsos, *Resistance of geopolymer and Portland cement based systems to silage effluent attack.* Cement and Concrete Research, 2017. **92**: p. 56-65.
40. Wang, Q., L. Li, C.P. Wu, and Z.T. Sui. *Research on adaptability of slag-based geopolymer with superplasticizer*. in *Key Engineering Materials*. 2009. Trans Tech Publ.

41. Nematollahi, B. and J. Sanjayan, *Effect of different superplasticizers and activator combinations on workability and strength of fly ash based geopolymer.* Materials & Design, 2014. **57**: p. 667-672.
42. C, A., *ASTM C1437-15 Standard Test Method for Flow of Hydraulic Cement Mortar.* Annual book of ASTM standards, 2015. **4**.
43. Okamura, H. and K. Ozawa, *Mix design for self-compacting concrete.* Concrete library of JSCE, 1995. **25**(6): p. 107-120.
44. ASTM, A., *C109/C109M-Standard Test Method for Compressive Strength of Hydraulic Cement Mortars (Using 2-in. or (50-mm) Cube Specimens); 2013. 2.* Scope of work shall include but not be limited to the following:-Suspended metal grid for acoustical tile ceiling system, 1999.
45. Committee, J.T., *AS 1012.11-2000 (R2014) Methods of testing concrete Determination of the modulus of rupture.* Australian Standard (AS), Joint Technical Committee BD-042, Australia, 2000.
46. Farina, I., M. Modano, G. Zuccaro, R. Goodall, and F. Colangelo, *Improving flexural strength and toughness of geopolymer mortars through additively manufactured metallic rebars.* Composites Part B: Engineering, 2018. **145**: p. 155-161.
47. ASTM, C., *642, Standard test method for density, absorption, and voids in hardened concrete.* Annual book of ASTM standards, 2006. **4**.
48. Ismail, I., S.A. Bernal, J.L. Provis, S. Hamdan, and J.S. van Deventer, *Drying-induced changes in the structure of alkali-activated pastes.* Journal of Materials Science, 2013. **48**(9): p. 3566-3577.
49. Bernal, S.A., E.D. Rodríguez, R. Mejía de Gutiérrez, and J.L. Provis, *Performance of alkali-activated slag mortars exposed to acids.* Journal of Sustainable Cement-Based Materials, 2012. **1**(3): p. 138-151.
50. Astm, C., *1585-04. Standard test method for measurement of rate of absorption of water by hydraulic-cement concretes.* ASTM International, 2004.
51. Albitar, M., M.M. Ali, P. Visintin, and M. Drechsler, *Durability evaluation of geopolymer and conventional concretes.* Construction and Building Materials, 2017. **136**: p. 374-385.
52. Deb, P.S., P. Nath, and P.K. Sarker, *Drying shrinkage of slag blended fly ash geopolymer concrete cured at room temperature.* Procedia Engineering, 2015. **125**: p. 594-600.
53. ASTM, C., *Standard Test Method for Length Change of Hardened Hydraulic-Cement Mortar and Concrete.* C157 / C157M - 08, 2014.
54. Zhang, W., Y. Hama, and S.H. Na, *Drying shrinkage and microstructure characteristics of mortar incorporating ground granulated blast furnace slag and shrinkage reducing admixture.* construction and building materials, 2015. **93**: p. 267-277.
55. Yang, L., Z. Jia, Y. Zhang, and J. Dai, *Effects of nano-TiO2 on strength, shrinkage and microstructure of alkali activated slag pastes.* Cement and Concrete Composites, 2015. **57**: p. 1-7.
56. Ariffin, N.F., M.W. Hussin, A.R.M. Sam, M.A.R. Bhutta, N.H.A. Khalid, and J. Mirza, *Strength properties and molecular composition of epoxy-modified mortars.* Construction and Building Materials, 2015. **94**: p. 315-322.
57. Ren, J., S.-Y. Guo, J. Su, T.-J. Zhao, J.-Z. Chen, and S.-L. Zhang, *A novel TiO2/Epoxy resin composited geopolymer with great durability in wetting-drying and phosphoric acid solution.* Journal of Cleaner Production, 2019.

58. Duran Atiş, C., C. Bilim, Ö. Çelik, and O. Karahan, *Influence of activator on the strength and drying shrinkage of alkali-activated slag mortar.* Construction and Building Materials, 2009. **23**(1): p. 548-555.
59. Kahraman, S. and R. Altindag, *A brittleness index to estimate fracture toughness.* International Journal of Rock Mechanics and Mining Sciences, 2004. **2**(41): p. 343-348.
60. Gunsallus, K.t. and F. Kulhawy. *A comparative evaluation of rock strength measures*. in *International Journal of Rock Mechanics and Mining Sciences & Geomechanics Abstracts*. 1984. Elsevier.
61. Committee, J.T., *AS 1012.21—1999 Methods of testing concrete Method 21: Determination of water absorption and apparent volume of permeable voids in hardened concrete* Australian Standard (AS), Joint Technical Committee BD-042, Australia, 1999.
62. Shaikh, F.U.A., *Mechanical and durability properties of fly ash geopolymer concrete containing recycled coarse aggregates.* International Journal of Sustainable Built Environment, 2016. **5**(2): p. 277-287.
63. Andrews-Phaedonos, F. *Assessment of concrete durability using a single parameter with a high level of precision: the VPV test*. in *ARRB Conference, 25th, 2012, Perth, Western Australia, Australia*. 2012.
64. Natarajan, S., N.N. Pillai, and S. Murugan, *Experimental Investigations on the Properties of Epoxy-Resin-Bonded Cement Concrete Containing Sea Sand for Use in Unreinforced Concrete Applications.* Materials, 2019. **12**(4): p. 645.
65. Pan, X., Z. Shi, C. Shi, T.-C. Ling, and N. Li, *A review on surface treatment for concrete–Part 2: Performance.* Construction and Building Materials, 2017. **133**: p. 81-90.
66. Aguirre-Guerrero, A.M., R.A. Robayo-Salazar, and R.M. de Gutiérrez, *A novel geopolymer application: Coatings to protect reinforced concrete against corrosion.* Applied Clay Science, 2017. **135**: p. 437-446.
67. Leung, C.K., H.-G. Zhu, J.-K. Kim, and R.S. Woo, *Use of polymer/organoclay nanocomposite surface treatment as water/ion barrier for concrete.* Journal of materials in civil engineering, 2008. **20**(7): p. 484-492.
68. Gao, X., Q. Yu, and H. Brouwers, *Reaction kinetics, gel character and strength of ambient temperature cured alkali activated slag–fly ash blends.* Construction and Building Materials, 2015. **80**: p. 105-115.
69. Collins, F. and J. Sanjayan, *Effect of pore size distribution on drying shrinking of alkali-activated slag concrete.* Cement and Concrete Research, 2000. **30**(9): p. 1401-1406.
70. Ye, H., C. Cartwright, F. Rajabipour, and A. Radlińska, *Understanding the drying shrinkage performance of alkali-activated slag mortars.* Cement and Concrete Composites, 2017. **76**: p. 13-24.
71. Ye, H. and A. Radlińska, *Shrinkage mechanisms of alkali-activated slag.* Cement and Concrete Research, 2016. **88**: p. 126-135.
72. Swain, M. *Toughening mechanisms for ceramics*. in *Proceedings of The 7th International Conference On Fracture (ICF7)*. 1989. Elsevier.
73. Boccaccini, A.R., M. Bücker, J. Bossert, and K. Marszalek, *Glass matrix composites from coal flyash and waste glass.* Waste management, 1997. **17**(1): p. 39-45.
74. Monette, L. and M. Anderson, *Effect of particle modulus and toughness on strength and toughness in brittle particulate composites.* Scripta Metallurgica et Materialia;(United States), 1993. **28**(9).

75. Shchipunov, Y.A. and T.y.Y. Karpenko, *Hybrid polysaccharide− silica nanocomposites prepared by the sol− gel technique.* Langmuir, 2004. **20**(10): p. 3882-3887.
76. Shchipunov, Y.A., *Sol–gel-derived biomaterials of silica and carrageenans.* Journal of colloid and interface science, 2003. **268**(1): p. 68-76.
77. Alehyen, S., M. Achouri, and M. Taibi, *Characterization, microstructure and properties of fly ash-based geopolymer.* J. Mater. Environ. Sci, 2017. **8**(5): p. 1783-1796.
78. Nayak, P.S. and B. Singh, *Instrumental characterization of clay by XRF, XRD and FTIR.* Bulletin of Materials Science, 2007. **30**(3): p. 235-238.
79. Zhang, Z., H. Wang, and J.L. Provis, *Quantitative study of the reactivity of fly ash in geopolymerization by FTIR.* Journal of Sustainable Cement-Based Materials, 2012. **1**(4): p. 154-166.
80. Nath, D., S. Bandyopadhyay, S. Gupta, A. Yu, D. Blackburn, and C. White, *Surface-coated fly ash used as filler in biodegradable poly (vinyl alcohol) composite films: Part 1—The modification process.* Applied Surface Science, 2010. **256**(9): p. 2759-2763.

Figure
Click here to download Figure: List of figures.doc

List of figures

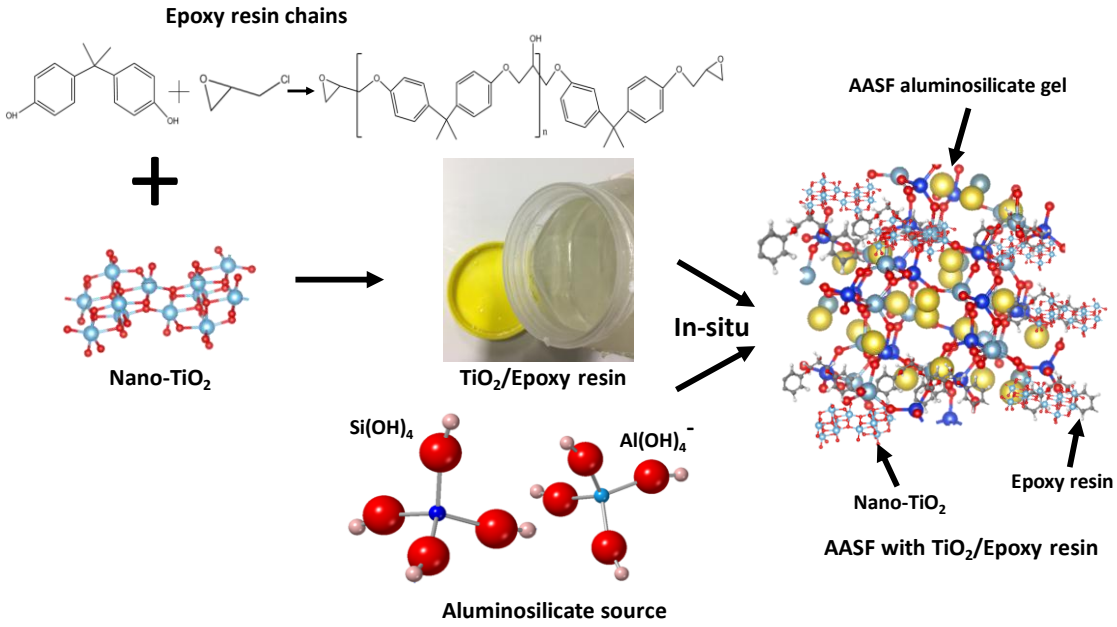

Fig. 1. Schematic diagram of the in-situ preparation and manufacturing process of the AASF paste composited by an inorganic-organic nano-TiO_2/Epoxy resin composite.

Fig. 2. The three-point flexural bending strength test with the testing machine and a prism paste sample while testing.

Fig. 3. A presentation of shrinkage measurements during the entire curing age.

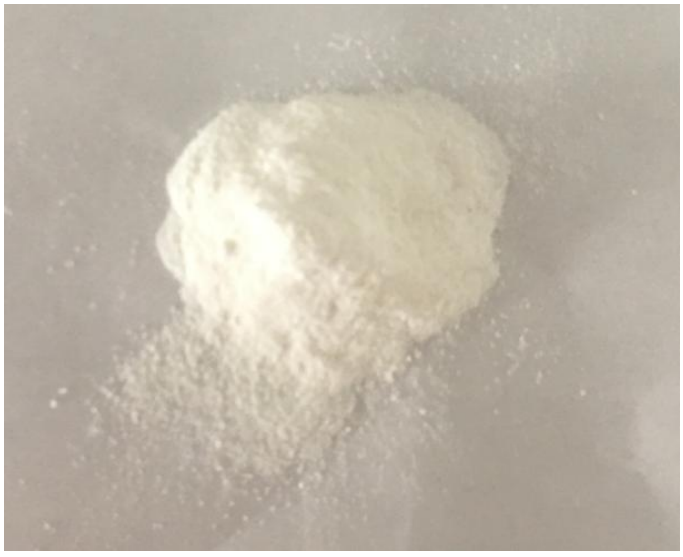

Fig. 4. The manufactured nano-TiO_2 particles shown in clusters.

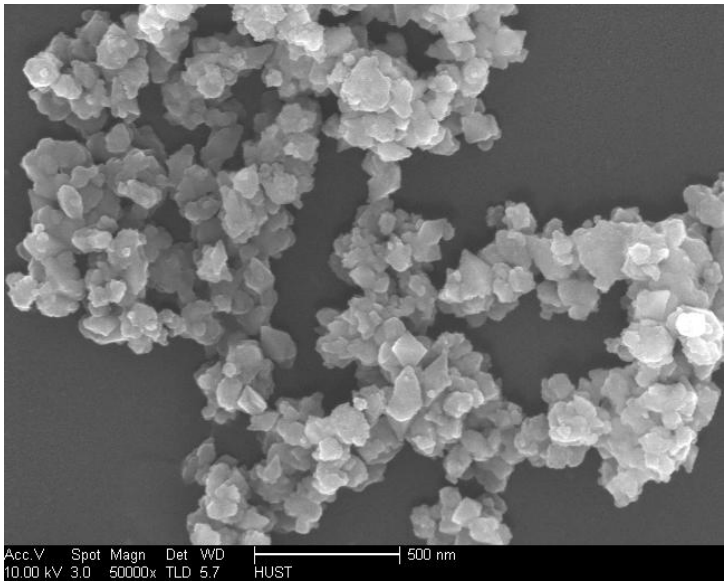

Fig. 5. A SEM image of the nano-TiO_2 particles in secondary electron mode.

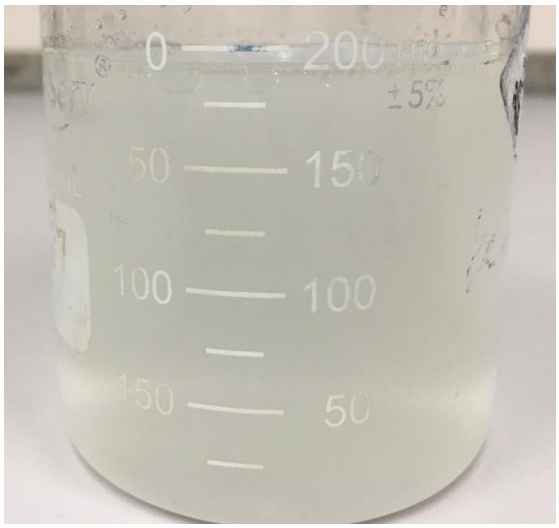

Fig. 6. The homogeneous liquid mixture of the nano-TiO_2/Epoxy resin and alkaline activator solution.

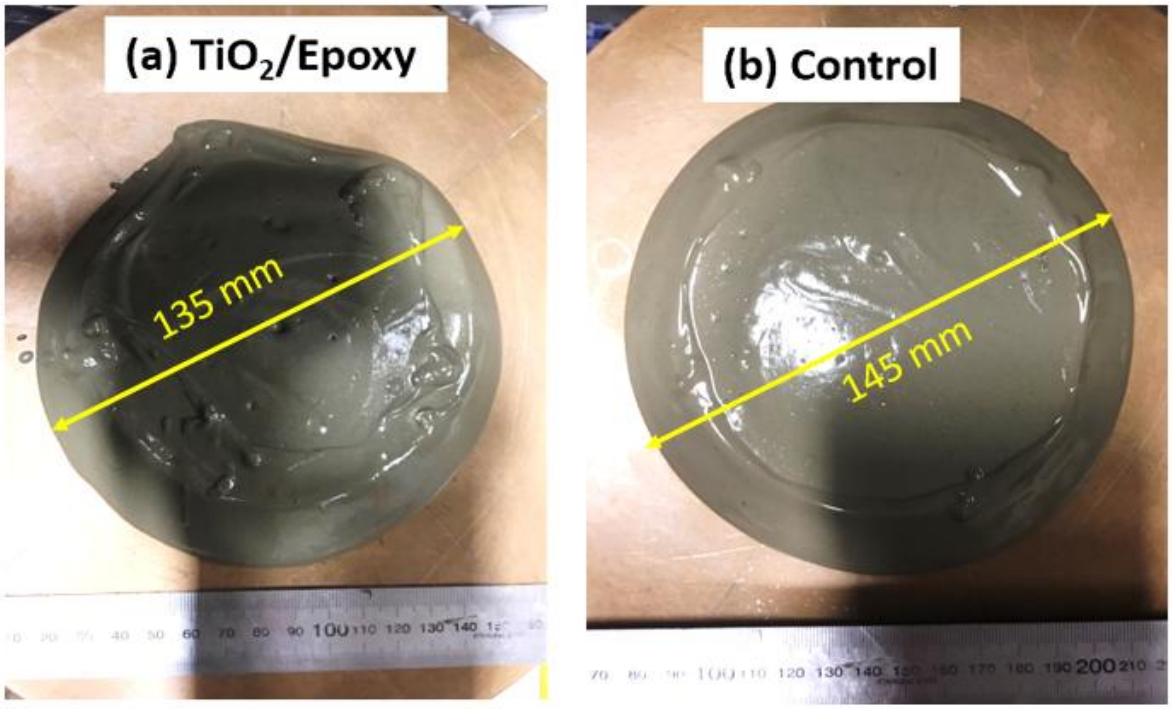

Fig. 7. The flowability of the newly-mixed pastes of the two mixes. (a) The TiO_2/Epoxy paste (containing 2% TiO_2/Epoxy resin by mass); (b) The control paste.

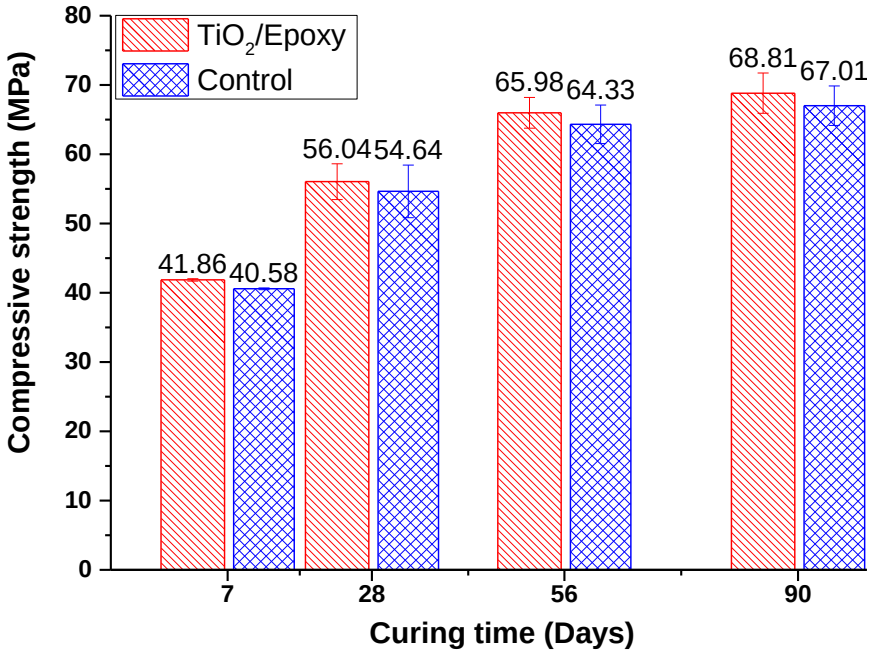

Fig. 8. Compressive strength evolution over different curing ages for the two mixes of paste samples.

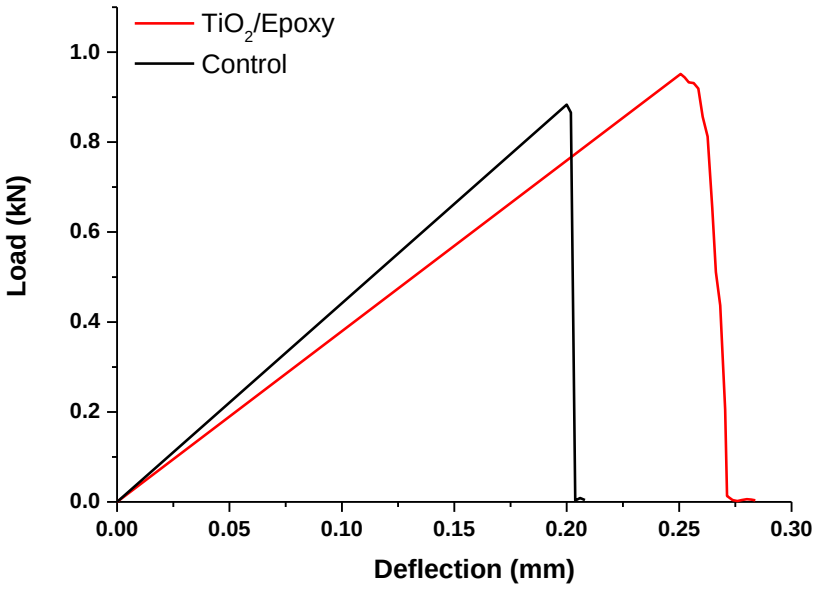

Fig. 9. The load-deflection curve obtained from the flexural bending strength test for the two paste mixes after 56 days of curing.

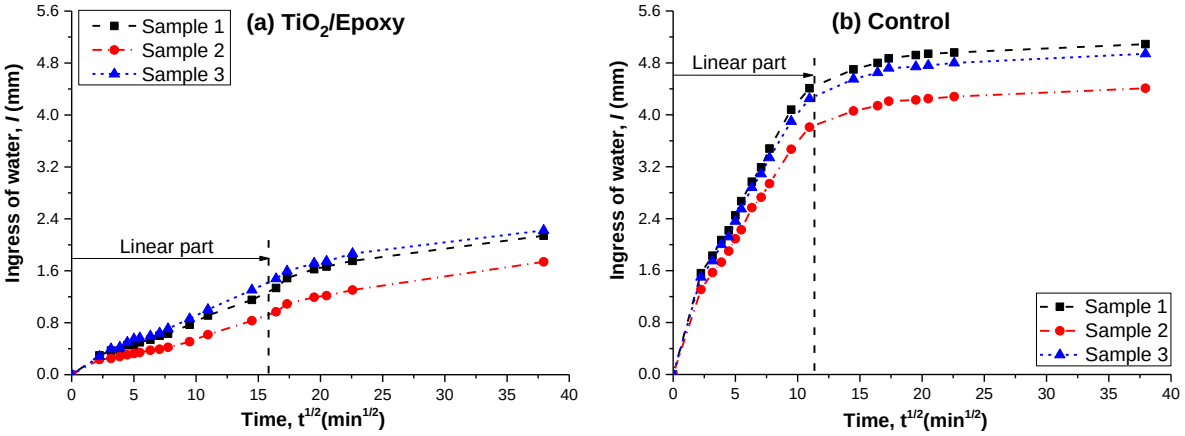

Fig. 10. The cumulative water absorption of the TiO_2/Epoxy AASF pastes (a) and control pastes (b) over the immersion period (24 hours) expressed as the square root of time. (Three replicates were tested for each mixture of pastes)

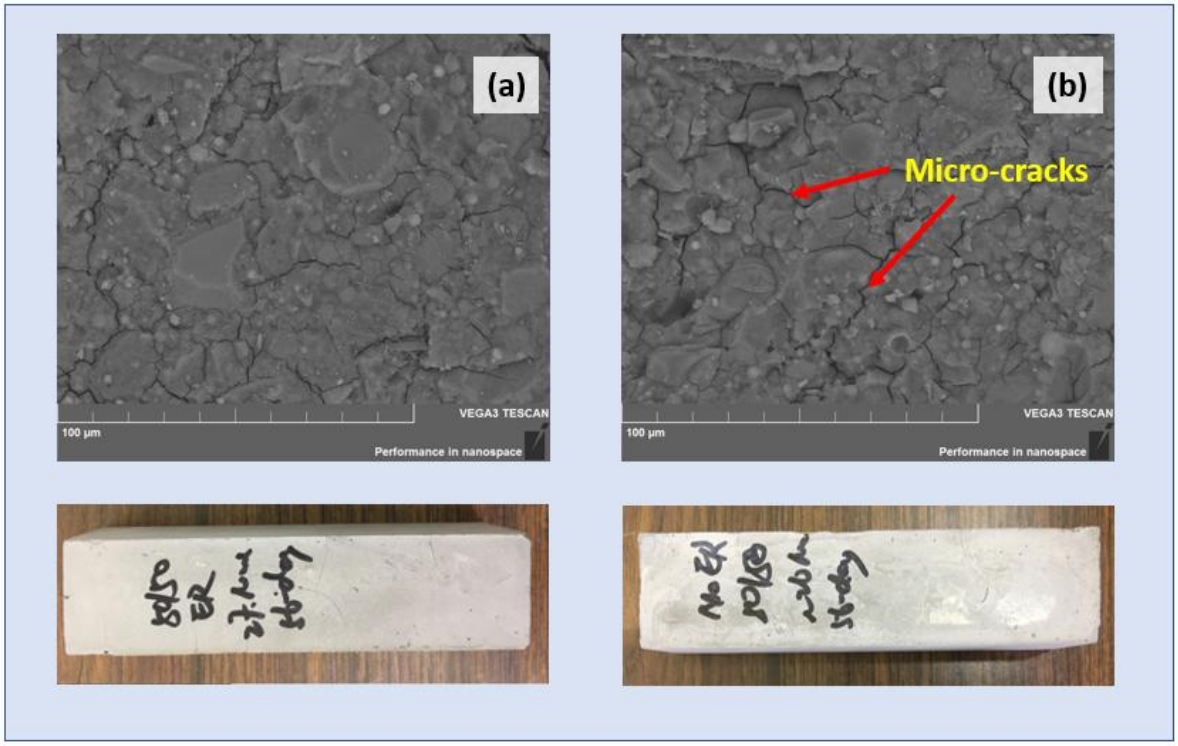

Fig. 11. SEM images of TiO_2/Epoxy AASF pastes (a) and control pastes (b) after 56-day curing.

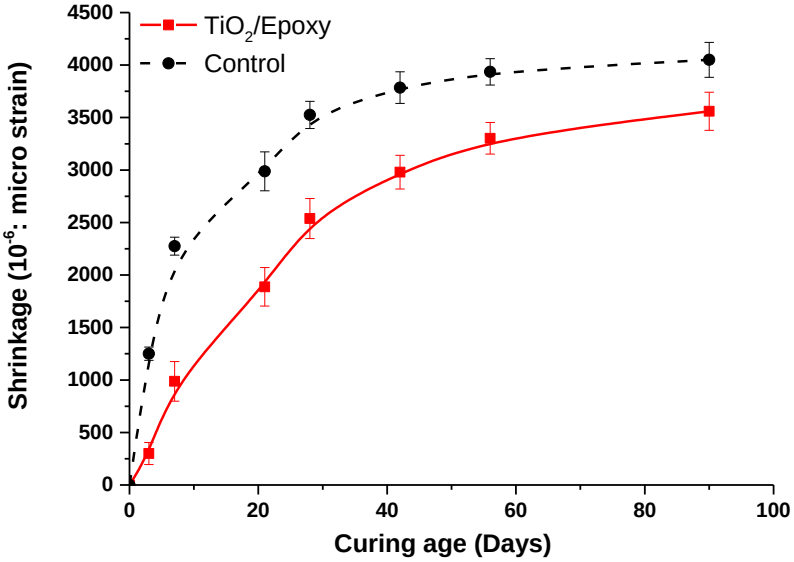

Fig. 12. Drying shrinkage of the TiO_2/Epoxy and control pastes over 90-day curing ages.